

RESEARCH ARTICLE

Extracting Lift and Drag Polars from Blade Resolved Computational Fluid Dynamics for use in Actuator Line Modelling of Horizontal Axis Turbines

A. Wimshurst and R. H. J. Willden

Department of Engineering Science, University of Oxford, Parks Road, Oxford, OX1 3PJ, UK.

ABSTRACT

Low order rotor models such as the actuator line method are desirable as an efficient method of computing the large range of operating and environmental conditions, required to design wind and tidal rotors and arrays. However, the integrated thrust and torque predictions for each rotor are dominated by the blade loading on the outboard sections, where three-dimensional (3D) effects become increasingly significant and the accuracy of the reduced order methods remains uncertain. To investigate the accuracy of the spanwise blade loading on an individual rotor, actuator line and blade boundary layer resolved computations of the Model Rotor Experiments in Controlled Conditions (MEXICO) rotor are presented. The high fidelity blade resolved simulations give good agreement with measured pressure coefficient and particle image velocimetry (PIV) data. Alternative lift and drag polars are extracted from the 3D simulated flow fields as a function of radial position. These are then used as replacement inputs for the actuator line method. Significant improvement in the accuracy of the actuator line predictions is found when using these 3D extracted polars, compared to using simulated two-dimensional (2D) lift and drag polars with empirical correction applied to the spanwise loading distribution. Additionally, the 3D flow field data is used to derive different axial and tangential spanwise loading corrections for use with the 2D blade polars. Copyright © 2016 John Wiley & Sons, Ltd.

KEYWORDS

Actuator Line Method, MEXICO, Tip Correction, Wind Turbine, CFD, OpenFOAM

Correspondence

Department of Engineering Science, University of Oxford, Parks Road, Oxford, OX1 3PJ, UK
E-mail: Aidan.Wimshurst@eng.ox.ac.uk

Received . . .

1. INTRODUCTION

The study of wind and tidal turbine rotors and their arrays requires multiple simulations to represent the diversity of operating and environmental conditions. For this reason, low order rotor models such as actuator line (AL) and embedded Reynolds-Averaged Navier-Stokes Blade Element methods (RANS-BEM), are desirable to satisfy the computational requirements. However, the accuracy of these methods for predicting rotor loading and the resulting flow field, can be highly dependant on the lift and drag polars that are used as a sub-grid model to avoid directly resolving the rotor blade boundary layers. The lift and drag polars are commonly derived from experimental measurements or two-dimensional (2D) computational fluid dynamics (CFD) computations of isolated non-rotating aerofoils, representing a given spanwise section of the rotor. Empirical correction factors calibrated using experimental data from available rotors are then applied to the blade loading distribution, to account for the three-dimensional (3D) effects that have not been captured.

In this article, a comparison will be made of three different actuator line computations. In the first, the lift and drag polars are taken directly from 2D computations of isolated non-rotating 2D aerofoil sections without empirical corrections. In the second, the same set of lift and drag polars are used but with the empirical ‘pressure equalisation’ correction of Shen et al. [1] applied to the blade loading distribution. This correction factor aims to represent the reduction in blade loading on the outboard sections as a result of the pressure equalisation between the pressure and suction surfaces, that must occur at the blade tip for a 3D blade. The third computation uses lift and drag polars extracted directly from the blade resolved

computations and thus includes all the 3D flow effects that are elsewhere included through empirical correction. The aim of this work will be to demonstrate that improved prediction of the axial and tangential forces on the blade outboard sections can be obtained by using lift and drag polars derived directly from blade resolved CFD. The improved axial and tangential force prediction subsequently results in more accurate prediction of the integrated rotor thrust and torque. Furthermore, this work should also complement recent studies on improving the accuracy of the actuator line method through careful choice of the mesh resolution and blade load smearing distribution, performed by Martínez-Tossas et al. [2] and Jha et al [3].

The article begins with a brief overview of the Model Rotor Experiments in Controlled Conditions (MEXICO) rotor that was used as a basis for comparison in this work, followed by a short discussion of the numerical method and validation of the blade boundary layer resolved computations. Subsequently, the lift and drag polars will be derived from the blade resolved computations and the three different actuator line computations will be performed. A comparison will then be made of the performance prediction of the actuator line computations, the blade resolved computations and the experimental measurements. To finish, some brief suggestions will be given for improving the method for future rotor computations and remaining areas of uncertainty will be highlighted.

2. MEXICO EXPERIMENTS

The development and validation of aerodynamic analysis tools using detailed measurements from full scale wind turbines can be challenging, due to variable environmental conditions that are difficult to recreate accurately. To address this difficulty, the MEXICO rotor experiments were designed with the aim of creating an extensive experimental data set under controlled conditions, to validate aerodynamic models. The experiments were carried out in the Large Low-speed facility (LLF) of the German-Dutch Wind Tunnels (DNW) in December 2006, in the 9.5m high by 9.5m wide open section of the tunnel. A large volume of data was recorded, which was subsequently analysed under the IEA Wind Task 29 Mexnext, as an international collaborative project. By the end of the first phase of the project in 2011, several aerodynamic codes had been successfully validated and key areas of uncertainty in these models were highlighted [4]. In June/July 2014, a second round of experimental measurements were taken on the MEXICO rotor, as part of a new MEXICO project within the European aerospace program ESWIRP. These new experiments were aimed at validating and complementing the original MEXICO measurements, along with addressing some of the remaining uncertainties. Some preliminary measurements have been reported by Boorsma and Schepers [5] and were used where available, as part of the validation exercise here.

The rotor used in the MEXICO experiments was a highly instrumented 3 bladed 4.5m diameter horizontal axis rotor, with a hub diameter of approximately 0.54m. The blades were constructed from three separate aerofoil sections, with the DU91-W2-250 from 20% to 46% of the span, the RISØ-A1-21 from 54% to 66% of the span, the NACA 64-418 from 74% to 100% of the span and proprietary transition pieces in between. More detailed information for the rotor geometry can be found in Schepers et al. [6]. For this investigation, the aerodynamic lift and drag coefficients for the transition pieces used in the actuator line computations were linearly interpolated from the aerodynamic data for the neighbouring aerofoil sections, following Shen et al. [7].

In total, 148 Kulite pressure sensors were placed along the blade surface at 5 independent spanwise sections of the blade (25%, 35%, 60%, 82% and 92% of the blade span), allowing the blade surface pressure distribution to be recorded. In addition to surface pressure measurements, stereo particle image velocimetry (PIV) measurements were taken in the vicinity of the rotor plane to complement the measured blade loading. These measurements represented a considerable addition to the data set and were the primary reason for selecting the MEXICO experiments over other experimental data sets, such as the NREL Phase VI rotor experiments [8].

During the MEXICO experiments, the rotor was operated at rotational speeds (ω) of 324.5 and 424.5 rpm and at yaw angles between $+30^\circ$ and -30° , for tunnel velocities (U_∞) between 10 and 24 m/s. A range of blade pitch angles from 5.3° towards stall to 1.7° towards feather, were also investigated. In this study, a small subset of the full range of rotor operating conditions were chosen for comparison. Freestream tunnel velocities of 10, 15 and 24 m/s were chosen at a rotational speed of 424.5 rpm, in order to achieve a wide range of tip speed ratios ($\lambda = 10.0, 6.67$ and 4.17) corresponding to a turbulent wake state, design condition and post stall operating conditions for the rotor. Axial flow conditions (zero yaw) and a constant blade pitch angle of 2.3 degrees towards stall were set for all computations. These operating conditions were specifically chosen to allow an additional comparison with the blade boundary layer resolved computations of Bechmann et al. [9]. As an extension to the experimental measurements taken at free stream tunnel velocities of 10, 15 and 24 m/s, tunnel velocities of 12.5 and 19.5 m/s (corresponding to tip speed ratios $\lambda = 8.0, 5.13$) were also computed in order to generate lift and drag polars over a wide range of angles of attack, for the actuator line computations.

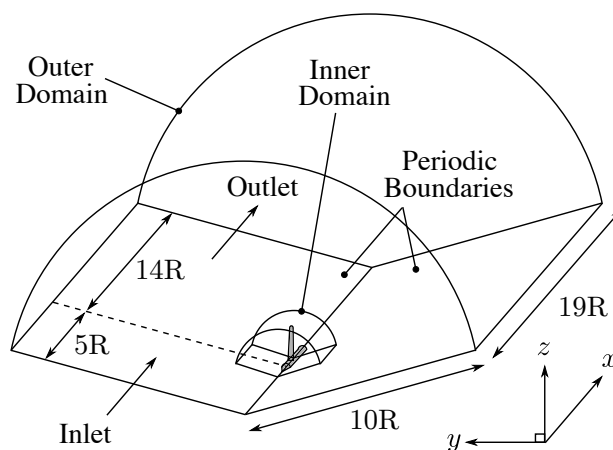


Figure 1. Diagram of the computational domain and the coordinate system adopted for the computations, highlighting the separate inner and outer domains. The streamwise flow direction is in the x direction and the rotor rotates clockwise.

3. COMPUTATIONAL DOMAIN AND MESHING STRATEGY

As the MEXICO rotor was placed in the open section of the DNW between the nozzle and collector, the effective blockage provided by the rotor was difficult to precisely define. Nevertheless, previous computations of the MEXICO rotor in unblocked conditions (less than 1%) and with the tunnel geometry included explicitly, concluded that blockage effects were insignificant [7]. For this investigation, the outer domain was therefore taken as a cylinder with radius $10R$ (where $R = 2.25\text{m}$ is the rotor radius), in order to ensure a low rotor blockage ratio of 1%. Previous investigations performed by Nishino and Willden [10] indicated that the effect of domain aspect ratio at low blockage ratios on device loading, was likely to be negligible. Therefore the approximation of the outer domain by a cylinder was not expected to influence the results appreciably. Furthermore, the cylindrical outer domain and omission of the tower geometry allowed rotational symmetry to be utilised, simplifying the meshing process and considerably reducing the computational time. Specifically, the computational domain was taken as a 120° wedge containing a third of the rotor, with periodic boundary conditions applied on either side. The blade geometry was reproduced accurately using the computer aided design (CAD) file provided as part of the MEXICO project, with a simplified nacelle based on the design drawings [6].

The overall domain was subdivided into an inner and outer domain, the inner of length $0.7R$ and radius $1.25R$ containing a single blade, nose cone and a section of the nacelle, and the outer containing the remainder of the nacelle and the domain boundaries. Fig 1 shows a simplified diagram of the computational domain layout, highlighting the inner and outer domains and the coordinate system adopted. The separate non conformal meshes for the inner and outer domain were joined by an arbitrary mesh interface (AMI) and coupling between the two meshes across the AMI was achieved using the face interpolation algorithm of Farrell and Maddison [11]. This domain decomposition into separate inner and outer domains allowed a refined block structured mesh to be applied in the inner domain, without incurring a significant increase in total cell count associated with continuing the blocks to the outer domain.

Within the inner domain, a C-C type blocking topology was adopted around the blade in order to retain the rotational symmetry at the sides of the 120° wedge and thus allow periodic boundary conditions to be applied. Several blocking slices were taken along the blade span, in order to capture the transition between the aerofoil sections and increase the spanwise resolution near the blade tip. Fig. 2 shows a horizontal slice through the blade at 82% of the span, demonstrating the C-C type blocking structure adopted for the coarse mesh. Finally, a Y block was included at the front of the nacelle in order to prevent highly distorted cells at the apex of the 120° wedge.

4. NUMERICAL METHOD

The multiple reference frame (MRF) approach of Luo et al. [12] was adopted for simulating rotor rotation. In the outer inertially fixed domain, the incompressible steady Reynolds-averaged Navier Stokes (RANS) equations were solved for the mean flow variables. Whereas in the inner domain containing the rotor, the incompressible steady RANS equations were solved in a rotating reference frame in terms of global (or absolute) velocities but with additional terms accounting for coriolis and centrifugal forces added to the equations, as additional source terms.

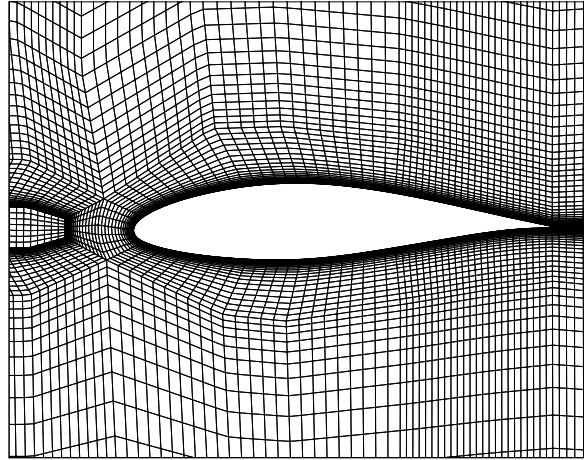


Figure 2. Slice through the coarse mesh at $r/R = 0.82$, demonstrating the C-C blocking topology around the NACA 64-418 aerofoil.

The governing equations were solved using the open source code OpenFOAM (version 2.3.1), which adopts a collocated cell centred approach for all flow variables and a face interpolation procedure in the style of Rhie and Chow [13], to prevent odd/even pressure decoupling. The governing equations were discretised using the second order finite volume method and formulated in terms of primitive (pressure-velocity) variables in a Cartesian coordinate system. The SIMPLE algorithm [14] was adopted for pressure-velocity coupling. Central differencing was applied for face interpolation of the Laplacian and gradient terms and the flux limited form of central differencing using the Sweby limiter [15], was applied for all the convection terms. Turbulence closure was achieved using the two equation $k - \omega$ SST turbulence model originally proposed by Menter [16] but with the updated model coefficients of Menter et al. [17], following current best practice.

Convergence to a quasi-steady solution was deemed to have occurred primarily by observing the integrated loads and near wake flow field using point probes. This typically occurred between 8000 and 12000 SIMPLE iterations. During these iterations, the residuals of the governing equations (normalised by their initial values) reduced by at least 5 orders of magnitude for the velocity components, 6 orders of magnitude for the turbulence scalars and 4 orders of magnitude for pressure. Relaxation factors were applied to artificially increase the diagonal dominance of the system and 2 non-orthogonal corrector loops were applied to the pressure corrector stage of the SIMPLE algorithm [18], in order to improve the numerical stability.

5. MESH SENSITIVITY

An initial (coarse) mesh was generated with chordwise and wall normal cell dimensions based on the results of preliminary 2D aerofoil computations of the NACA 64-418 aerofoil at a chord based Reynolds number of 0.7×10^6 (corresponding to the chord based Reynolds number at 82 % of the blade span, for the MEXICO rotor operating at the design condition). The spanwise cell dimensions were initially chosen based on prior experience with rotors from other investigations. This coarse mesh was selectively refined in the chordwise, spanwise and wall normal direction simultaneously, generating medium and fine meshes. Table I provides a summary of the generated meshes, including the chordwise spacing at the leading edge (LE), trailing edge (TE), the wall adjacent cell centroid height (y), the number of chordwise cells along the pressure and suction surfaces individually (N_c), the growth ratio normal to the wall (G), the number of spanwise cells (N_s), the spanwise cell dimension at the blade tip (Δ_{tip}) and the total number of cells in the inner domain (N_{cells}).

Table I. Summary of the mesh parameters adopted for the coarse, medium and fine meshes.

Mesh	LE [m]	TE [m]	y [m]	N_c	G	N_s	Δ_{tip} [m]	N_{cells}
Coarse	1.3e-3	1e-3	3e-5	58	1.2	130	2.2e-3	5,749,953
Medium	1.3e-3	5e-4	3e-5	78	1.1	188	1.5e-3	9,792,087
Fine	1.3e-3	2.5e-4	3e-5	98	1.075	210	1.0e-3	14,209,871

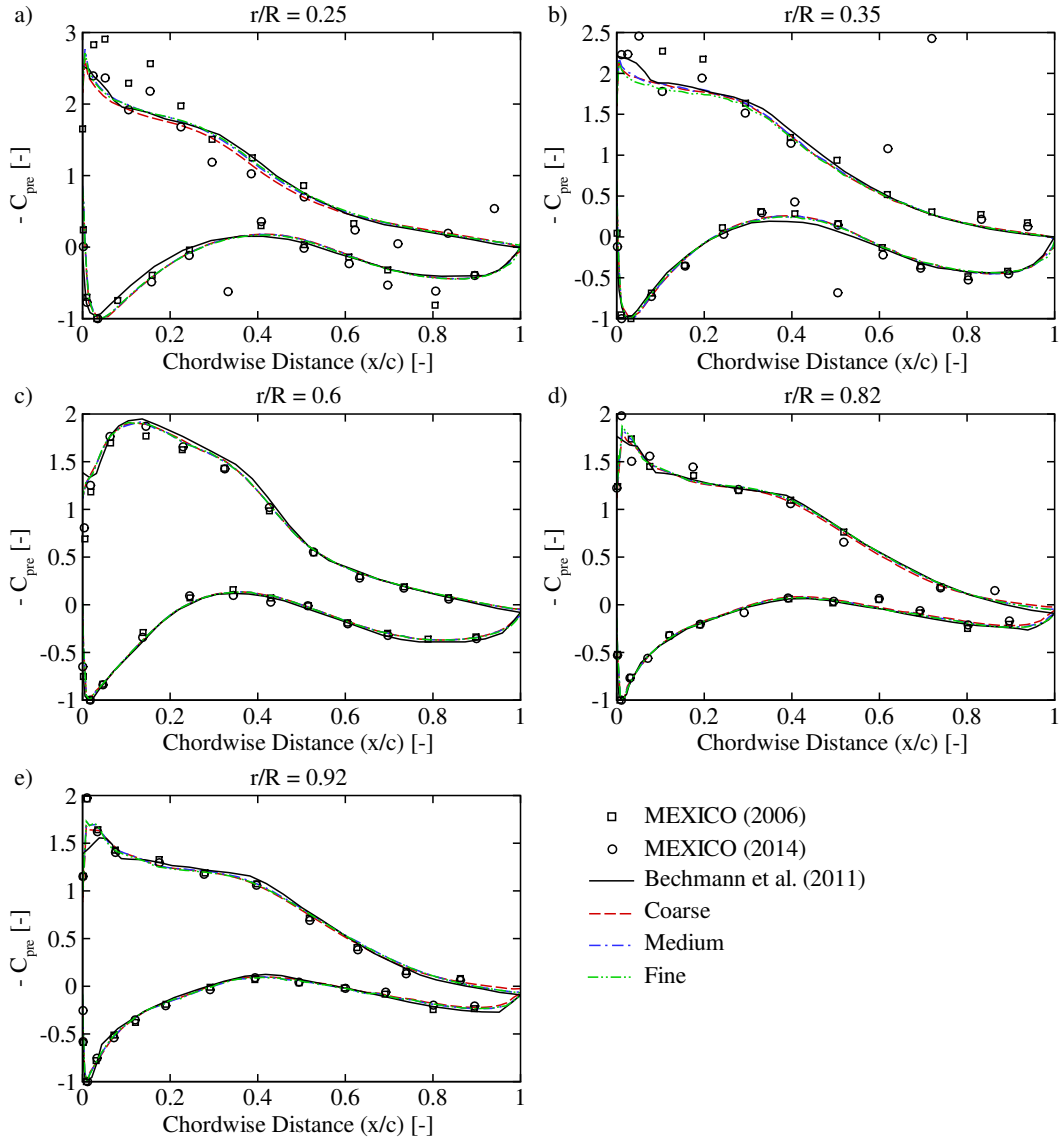


Figure 3. Surface pressure coefficient for the coarse, medium and fine meshes at the design condition ($U_{\infty} = 15.0$ m/s, $\lambda = 6.67$).

The wall normal distance (y) was selected to maintain a value of $y^+ < 5$ over the entire blade surface (where $y^+ = y\sqrt{\tau_w/\rho}/\nu$, τ_w is the wall shear stress, $\rho = 1.225$ kg/m³ is the fluid density and $\nu = 1.456 \times 10^{-5}$ m²/s is the kinematic viscosity) and hence resolve the boundary layer through to the viscous sub layer. A further reduction in wall normal distance to achieve a wall resolution of $y^+ \sim 1$ was simply not feasible to obtain without generating poor quality cells near the highly twisted blade root. Therefore the wall normal resolution was clearly sub-optimal but was nevertheless found to give sufficiently accurate results when compared with the experimental measurements and the blade resolved computations of Bechmann et al. [9].

5.1. Surface Pressure Coefficient

The coarse, medium and fine meshes were simulated at the high tip speed ratio ($U_{\infty} = 10.0$ m/s, $\lambda = 10.00$), design condition ($U_{\infty} = 15.0$ m/s, $\lambda = 6.67$) and low tip speed ratio ($U_{\infty} = 24.0$ m/s, $\lambda = 4.17$) operating conditions and then compared to identify the degree of sensitivity to mesh refinement. Fig. 3 compares the computed pressure coefficient (C_{pre}) with the original experimental measurements presented by Schepers et al. [4], the blade resolved computations of Bechmann et al. [9] and the new experimental measurements reported by Boorsma and Schepers [5] at the design

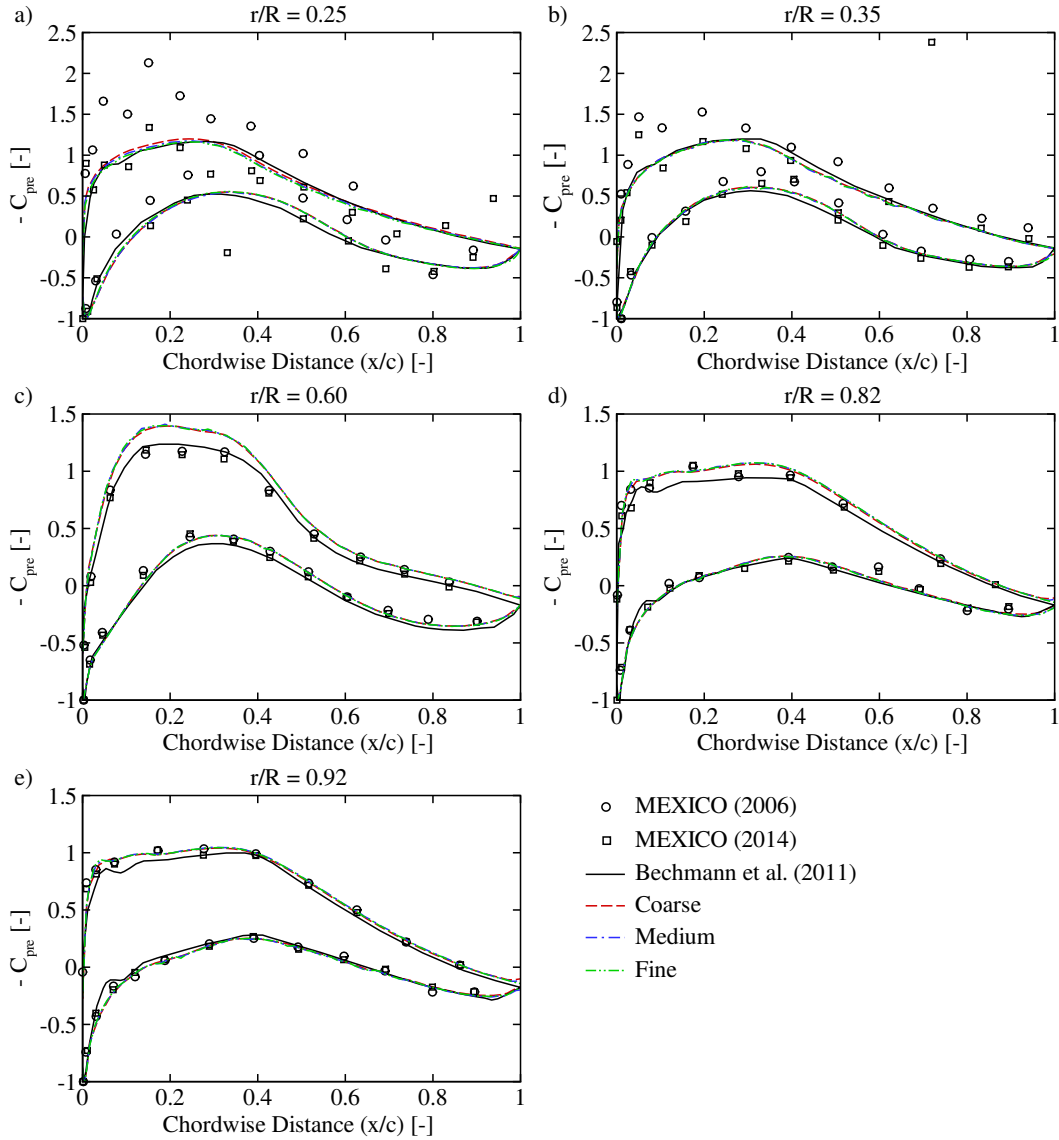


Figure 4. Surface pressure coefficient for the coarse, medium and fine meshes for the high tip speed ratio case ($U_\infty = 10.0$ m/s, $\lambda = 10.0$).

condition ($U_\infty = 15.0$ m/s, $\lambda = 6.67$). In Fig. 3, MEXICO (2006) refers to the original experimental measurements, whereas MEXICO (2014) refers to the new experimental measurements. For comparison with Bechmann et al. [9], the pressure coefficient has been defined based on the free stream dynamic pressure and then normalised to achieve a value of 1 at the stagnation point.

$$C_{pre} = \frac{p - p_\infty}{\frac{1}{2} \rho U_\infty^2} \quad (1)$$

Overall the coarse, medium and fine meshes appeared well converged over all the considered spanwise stations, with a maximum difference of 0.12 in the computed pressure coefficient occurring at $r/R = 0.25$ and $x/c = 0.38$ on the suction surface (a percentage difference of 4.8% when normalised by the maximum pressure coefficient magnitude of 2.57). Good agreement was also obtained with the blade resolved computations of Bechmann et al. [9] and the experimental measurements, particularly at the mid span ($r/R = 0.60$) and the outboard sections ($r/R = 0.82, 0.92$). The new and original experimental measurements also showed good agreement with each other, particularly for the outboard sections ($r/R = 0.82, 0.92$), leading to confidence in using these results to assess the computational predictions. However

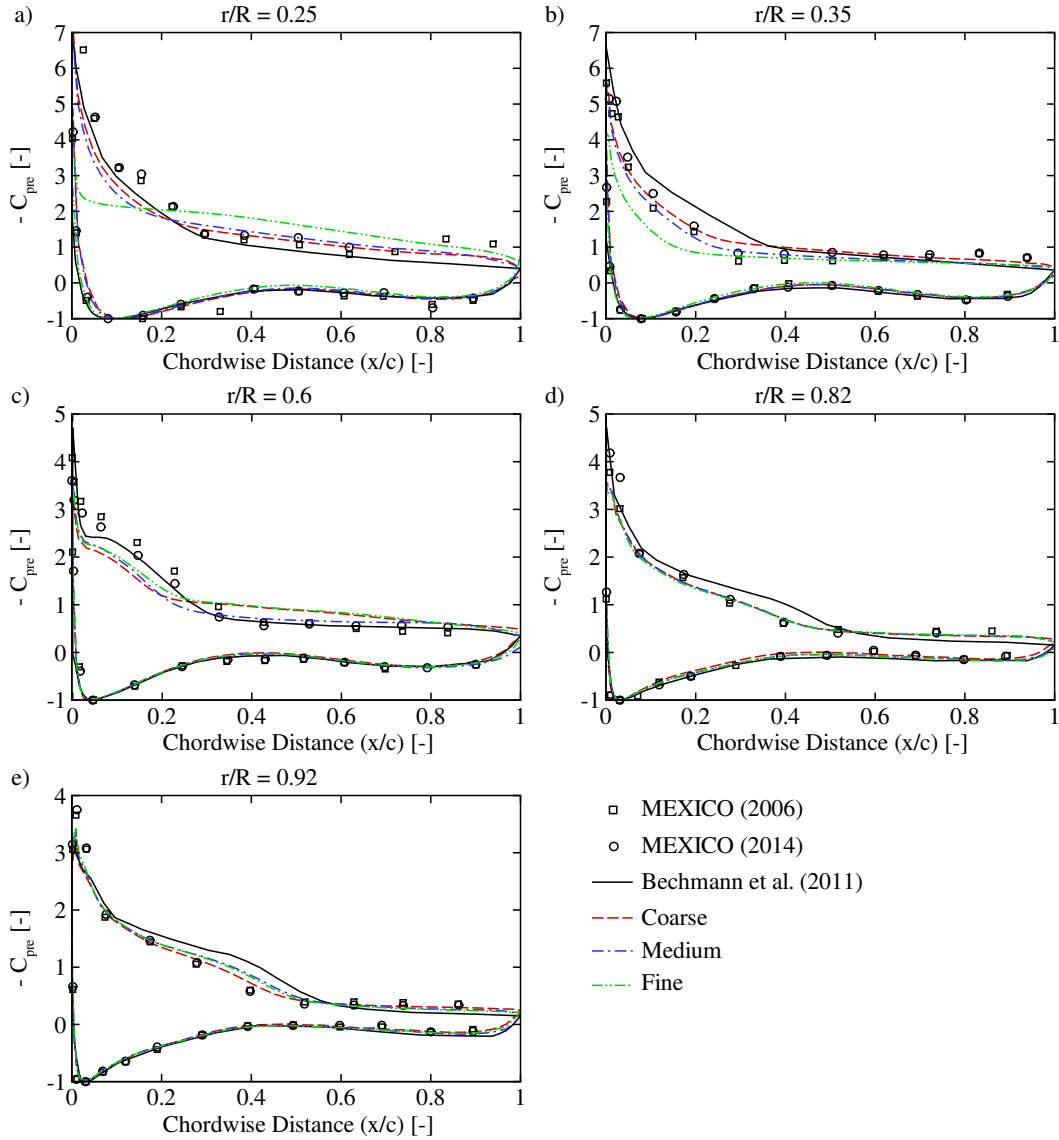


Figure 5. Surface pressure coefficient for the coarse, medium and fine meshes for the low tip speed ratio case ($U_\infty = 24.0$ m/s, $\lambda = 4.17$).

measurements of the inboard sections ($r/R = 0.25, 0.35$) seemed far less reliable, despite several faulty inboard sensors being repaired since the original experiments [5]. The accuracy of the computational predictions could therefore not be rigorously assessed for the inboard sections.

Good agreement was also found between the coarse, medium and fine meshes at the high tip speed ratio ($U_\infty = 10.0$ m/s, $\lambda = 10.0$), as shown in Fig. 4. In addition, both the computations presented here and those of Bechmann et al. [9] gave good agreement with the experimental measurements and with each other. Once again however, the original and new experimental results showed poor agreement with each other for the inboard sections ($r/R = 0.25, 0.35$) and hence the accuracy of the results could not be reliably assessed here.

Fig. 5 shows the surface pressure coefficient computed with the coarse, medium and fine meshes for the low tip speed ratio case ($U_\infty = 24.0$ m/s, $\lambda = 4.17$). The nearly constant pressure region on the rear half of the suction surface immediately indicated that heavy stall had occurred along the majority of the blade surface, for both the computations and the experimental measurements. Whilst the steady MRF approach was able to predict the surface pressure coefficient reasonably accurately at the higher tip speed ratios (where the flow remained attached), its accuracy was questionable here due to flow unsteadiness and hence the results should be interpreted cautiously. For this investigation, the actuator line

computations were performed at high tip speed ratios where the flow remained fully attached and hence the lift and drag polars derived from the low tip speed ratio case were not required anyway. The results shown here should be therefore only be interpreted as highlighting the limits of applicability of the method.

5.2. Spanwise Blade Loading

In order to determine the spanwise variation of the blade loading (for deriving the lift and drag polars), the blade was divided into 40 independent spanwise sections, clustered in a cosine distribution towards the root and the tip. At each of these sections, the pressure and wall shear stress were integrated in the chordwise direction and resolved in the global coordinate system to produce the spanwise variation of the axial and tangential forces per unit span (F_{ax} and F_t). Here the axial force refers to the force component parallel with the global x axis and the tangential force the force component parallel to the global $-y$ axis, rather than a coordinate system aligned with the local chord line. Therefore, the axial and tangential forces represent the thrust producing force and the torque producing force acting on the rotor.

Fig. 6 shows the axial and tangential forces computed with the coarse, medium and fine meshes for the high tip speed ratio ($U_\infty = 10.0$ m/s, $\lambda = 10.0$), design condition ($U_\infty = 15.0$ m/s, $\lambda = 6.67$) and low tip speed ratio ($U_\infty = 24.0$ m/s, $\lambda = 4.17$) operating conditions, along with the experimental measurements. Excellent agreement was observed between the coarse, medium and fine meshes along the entire span for the high tip speed ratio and at the design condition, with the coarse mesh slightly under predicting the axial and tangential forces near the root and tip. For the low tip speed ratio case ($U_\infty = 24.0$ m/s, $\lambda = 4.17$) the coarse, medium and fine meshes did not show converged axial or tangential forces along the blade span. This discrepancy was due to the steady flow solver being unable to accurately capture the unsteady separation process along the entire blade span (indicated by the relatively constant pressure region on the suction surface for all the spanwise sections shown in Fig. 5). However as noted previously, the actuator line computations in this investigation were not performed in the post stall region and hence the lift and drag polars derived from this computation, were not of primary importance.

Table II. Integrated rotor thrust and torque for the coarse, medium and fine meshes at the high tip speed ratio ($U_\infty = 10.0$ m/s, $\lambda = 10.0$) and design ($U_\infty = 15.0$ m/s, $\lambda = 6.67$) operating conditions.

	Tip Speed Ratio (λ) [-]	Thrust [N]	Torque [Nm]
MEXICO	10.0	854.0	61.1
Coarse	10.0	974.2	70.6
Medium	10.0	978.5	70.7
Fine	10.0	986.9	73.6
MEXICO	6.67	1516.8	284.6
Coarse	6.67	1678.3	320.8
Medium	6.67	1704.3	329.5
Fine	6.67	1713.5	329.5

Table II compares the rotor thrust and torque, computed by integrating the axial and tangential forces shown in Fig. 6, along the blade span for the high tip speed ratio case ($U_\infty = 10.0$ m/s, $\lambda = 10.0$) and at the design condition ($U_\infty = 15.0$ m/s, $\lambda = 6.67$). For the experimental measurements, a linear variation was assumed between the spanwise stations, with zero axial and tangential force assumed at the root and tip [4]. The coarse, medium and fine meshes were all found to over predict the integrated thrust and torque when compared with the MEXICO measurements at both tip speed ratios. Furthermore, with increasing mesh refinement the blade resolved computations were found to slightly increase the rotor thrust and torque, moving further away from the experimental predictions. However in this case, the experimental measurements should not automatically be assumed to be more reliable than the blade resolved computations, due to the sparsity of the chordwise and spanwise measurements that were taken. With 10-14 pressure taps on the pressure and suction surface at each station and only 5 spanwise stations, the integration procedure was likely to have incurred significant error. In particular, Schepers et al. [4] showed that adopting a non-linear variation of the axial force per unit span between the spanwise measurement stations, resulted in an increase in integrated thrust of up to 15% (a total thrust of 982.1N for the high tip speed ratio case and 1744.3N for the design tip speed ratio) when compared to the linear variation. To help address this uncertainty, Bechmann et al. [9] provided an additional estimate of the rotor thrust, by subtracting an estimate of the tower drag from the measured force balance at the base of the tower. Unfortunately, the tower drag could only be estimated based on the rotor wake reduced flow velocity approaching the upper section of the tower. The rotor thrust computed using this method (932N at the high tip speed ratio and 1661N at the design tip speed ratio) was estimated to be higher than predicted by integrating the pressure tap measurements and was therefore much closer to the blade resolved computations carried out here.

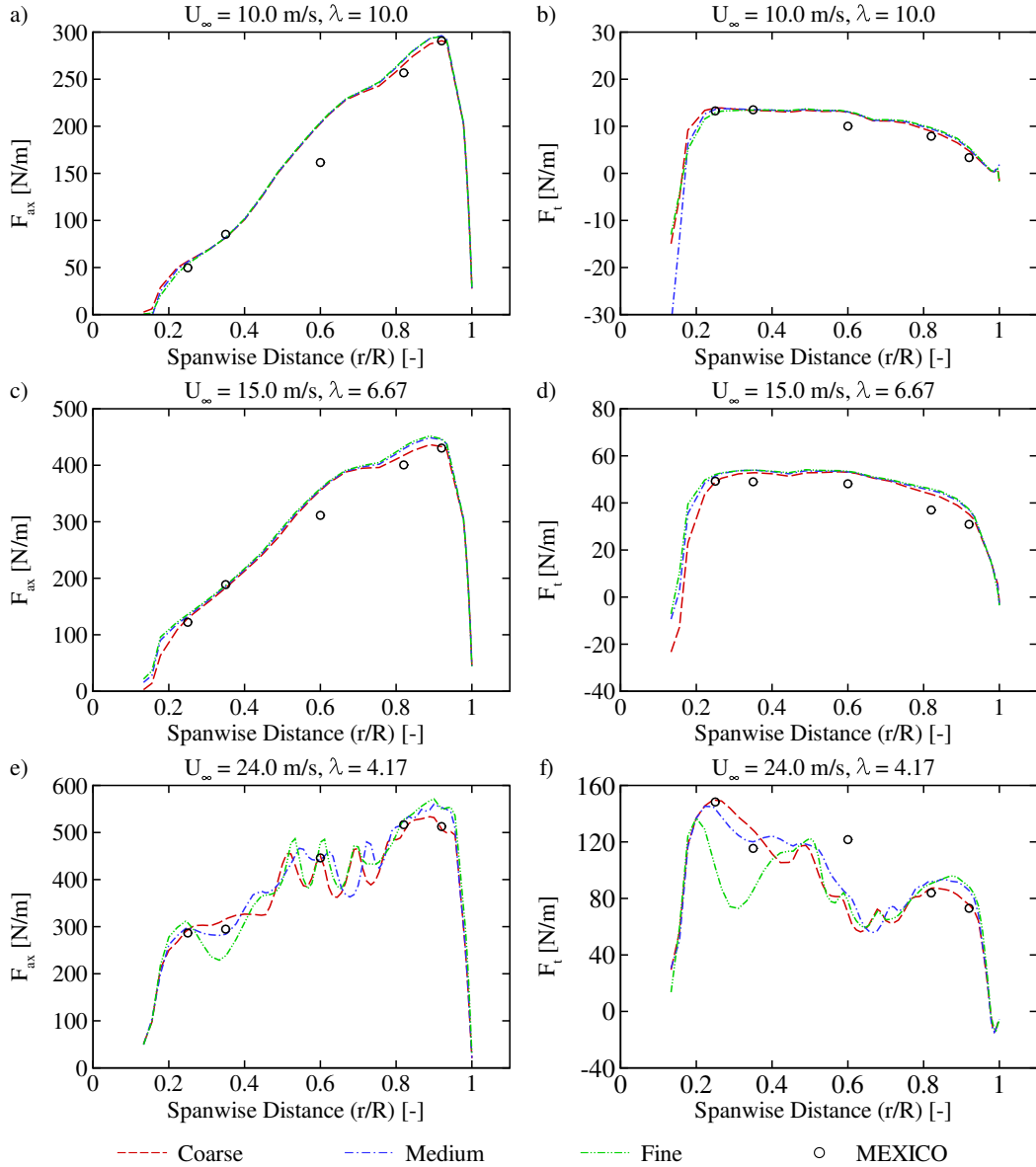


Figure 6. Axial and tangential blade forces per unit span for freestream velocities of 10.0 m/s (a and b), 15.0 m/s (c and d) and 24.0 m/s (e and f), computed with the coarse, medium and fine meshes.

Consequently it is difficult to draw definitive conclusions for the accuracy of the blade resolved computations, based on the integrated forces alone. Comparing the blade surface pressure measurements was deemed to be a more reliable assessment of mesh convergence and agreement with the experimental measurements. In the next section, an additional comparison is presented between the computed near wake flow field and the experimental PIV measurements, to complement the blade surface pressure coefficient comparisons and to assess the fidelity of the near wake flow field.

5.3. Near Wake Flow Field

Fig. 7 shows a schematic diagram of the full extent of the PIV measurements, with the origin of the coordinate system taken at the apex of the rotor. Note that only a small subset of the large volume of PIV data recorded in the original MEXICO experiments was used here for analysis. The measurements extended in a horizontal plane from $x = -4.5\text{m}$ ($2R$) upstream of the rotor to $x = 5.9\text{m}$ ($2.62R$) downstream of the rotor and in the lateral direction from $y = 1.18\text{m}$ ($0.52R$) to $y = 2.75\text{m}$ ($1.2R$). The lateral extent of the measurements allowed the flow around the outboard sections of the rotor

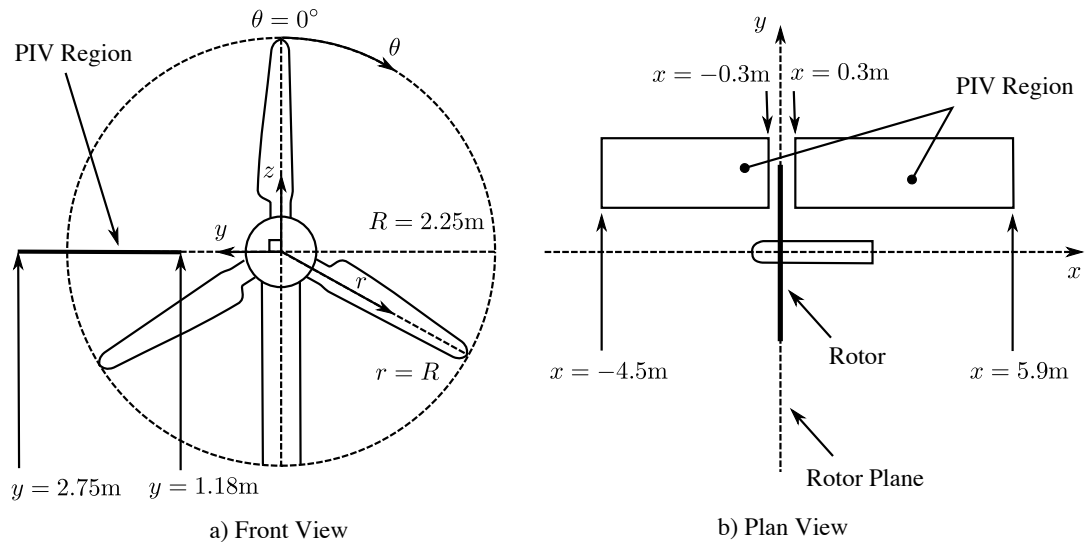


Figure 7. Schematic diagram showing the extent of the experimental PIV measurements from (a) the front view and (b) the plan view. The streamwise flow direction is in the x direction and the rotor rotates clockwise.

to be captured up to $x = -0.3\text{m}$ ($0.13R$) upstream and $x = 0.3\text{m}$ ($0.13R$) downstream of the rotor plane. Instantaneous PIV measurements were taken in these regions for rotor azimuthal positions of $\theta = 0^\circ, 20^\circ, 40^\circ, 60^\circ, 80^\circ, 100^\circ$ and 120° . Further details of the PIV measurement and analysis procedure can be found in Schepers et al. [4].

Fig. 8 shows the velocity components extracted from the blade resolved computations along a radial traverse $x = 0.3\text{m}$ ($0.13R$) downstream of the rotor, for rotor azimuthal positions of $\theta = 0^\circ$ and 120° . This azimuthal position was chosen as a check of the experimental measurements, which should have been the same due to the 120° rotational periodicity. The other rotor azimuthal positions were also compared ($\theta = 20^\circ, 40^\circ, 60^\circ, 80^\circ, 100^\circ$) but are not shown here as they showed the same qualitative behaviour. As pointed out by Bechmann et al. [9], the freestream axial velocity incident on the rotor (U_x) was lower in the experiments than the computations, despite a consistent tunnel velocity of $U_\infty = 15.0\text{ m/s}$. This was likely to be a result of the open tunnel configuration adopted for the experiments, allowing partial expansion of the incoming streamtube between the nozzle and the collector, thus leading to a small reduction in axial velocity incident on the rotor. For this reason, the axial velocity U_x in Fig. 8 has been non-dimensionalised by a reference velocity U_{ref} taken one diameter upstream of the rotor (14.3 m/s for the experiments and 14.7 m/s for the computations) in order to compare the velocity deficit imparted on the flow by the rotor between the experiments and the computations.

As shown in Fig. 8, the experimental PIV measurements for $\theta = 0^\circ$ and 120° showed excellent agreement, leading to increased confidence in using these experimental measurements for assessing the computed velocity components in the near wake. In addition, the blade resolved computations gave good qualitative agreement with each other and with the experimental measurements for all three velocity components along the entire traverse. The lateral velocity (U_y) was particularly well predicted. The streamwise velocity component (U_x) also qualitatively followed the experimental results well along the extent of the PIV traverse, increasing confidence in the blade resolved computations. However, the axial velocity measured in the experiments was universally lower than predicted by the computations along the entire PIV traverse. This implied that the force applied to the flow by the rotor should have been greater in the experiments than the computations, in direct contradiction with the spanwise blade loading results shown in Fig 6. Such findings have also been reported by Wimshurst and Willden [19], Shen et al. [7] and Schepers et al. [4] and has been identified as a key area of uncertainty to be addressed in the second round of MEXICO experiments [5].

At this stage, until the emergence of more experimental data, the computational results were deemed to be more reliable for assessing the blade loading than the experimental results. In addition, the computational results were deemed to be sufficiently converged with a moderate level of mesh refinement (the medium mesh) and were deemed to be acceptable for extracting lift and drag polars for actuator line computations, before the onset of stall. In the next section, the lift and drag polars will be extracted from the blade resolved computations and the actuator line computations subsequently performed.

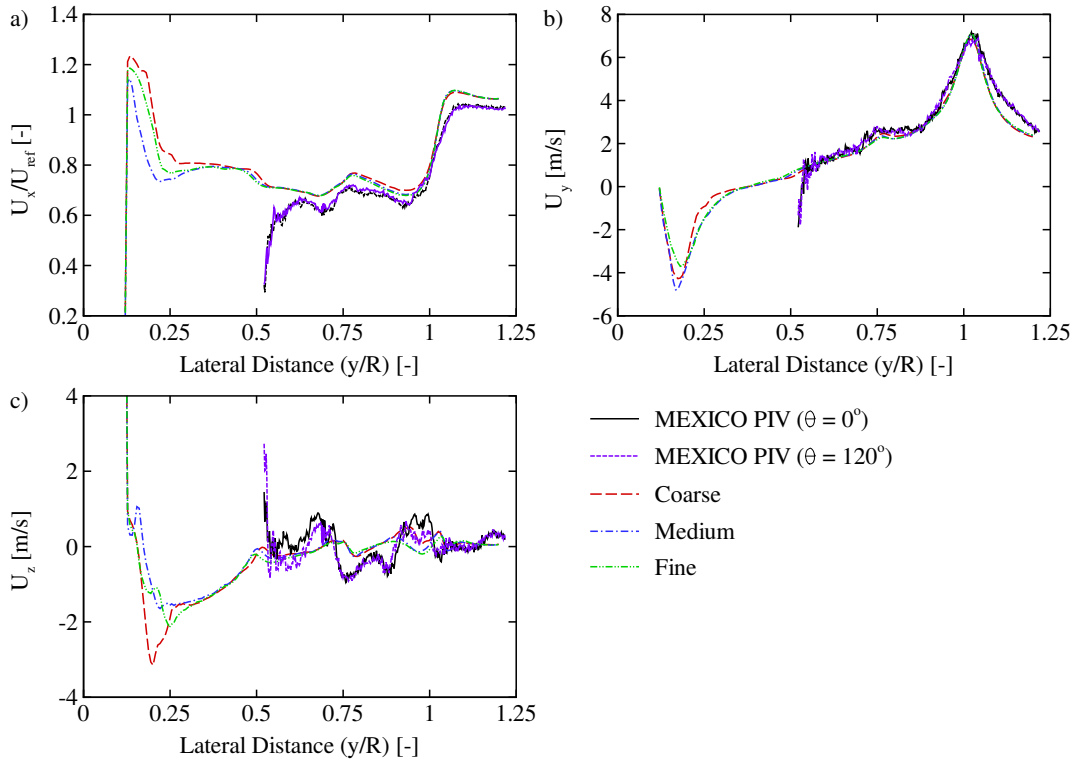


Figure 8. Radial PIV traverses $x = 0.3\text{m}$ ($0.13R$) downstream of the rotor plane for rotor azimuthal positions of $\theta = 0^\circ$ and 120° , at the design condition ($U_\infty = 15.0\text{ m/s}$, $\lambda = 6.67$) for the coarse, medium and fine meshes. The reference velocity has been taken as $U_{\text{ref}} = 14.3\text{ m/s}$ for the experiments and $U_{\text{ref}} = 14.7\text{ m/s}$ for the computations.

6. LIFT AND DRAG POLARS

In order to extract lift and drag polars from the blade resolved computations, the angle of attack (α), lift coefficient (C_L), drag coefficient (C_D) and relative velocity (U_{rel}) were required along the entire blade span. As the spanwise variation of axial and tangential forces per unit span (F_{ax} and F_t) on the blade were already computed in the previous section (by integrating the surface pressure and wall shear stress in the chordwise direction at each spanwise section), the problem reduced to extracting the angle of attack and relative velocity at each spanwise section. Once these quantities were determined, using the blade element diagram shown in Fig. 9, the lift and drag forces per unit span (L and D) could then be readily obtained by rotating the axial and tangential forces per unit span by the relative flow angle ϕ .

$$L = F_{\text{ax}} \cos(\phi) + F_t \sin(\phi) \quad (2)$$

$$D = F_{\text{ax}} \sin(\phi) - F_t \cos(\phi). \quad (3)$$

Once the lift and drag forces per unit span were computed, the sectional lift and drag coefficients were then evaluated using the relative velocity and the local chord length c ,

$$C_L = \frac{L}{\frac{1}{2} \rho U_{\text{rel}}^2 c} \quad (4)$$

$$C_D = \frac{D}{\frac{1}{2} \rho U_{\text{rel}}^2 c}. \quad (5)$$

However, the angle of attack and relative velocity are not straightforward to extract accurately from a rotating rotor blade. This is primarily because the angle of attack is a 2D concept, where each 2D blade segment is assumed to act independently of the others, neglecting the spanwise flow component. It should therefore be emphasised that all methods used to compute the angle of attack for rotating blades are only approximate, due to the inherent errors in reducing a 3D rotor blade into independent 2D blade segments. Furthermore, when using the extracted angle of attack to derive lift and

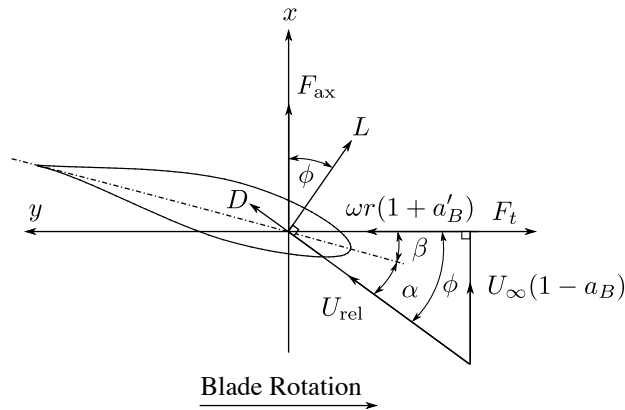


Figure 9. Blade element diagram for a spanwise section at radius r along the MEXICO blade. a_B and a'_B represent the axial and swirl induction factors at the blade section.

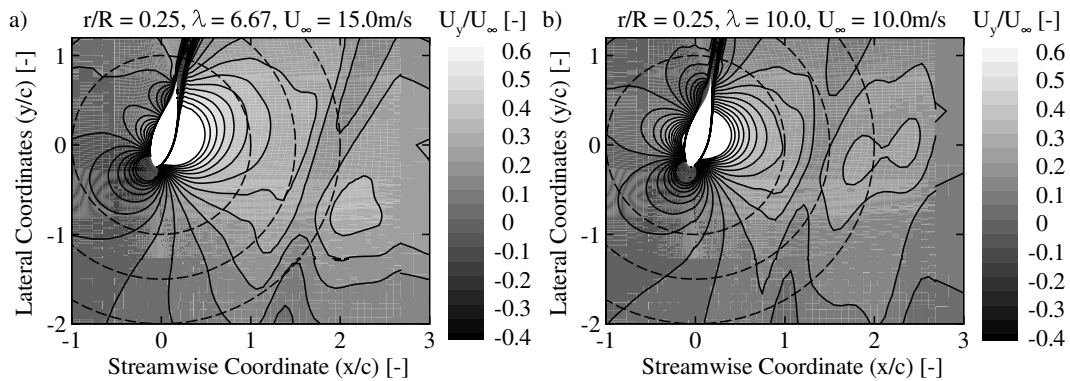


Figure 10. Contours of the lateral velocity component U_y (relative to the blade) on a horizontal slice $z = 0.5625\text{m}$ along the blade ($r/R = 0.25$), for (a) the design tip speed ratio ($U_\infty = 15.0\text{ m/s}$, $\lambda = 6.67$) and (b) the high tip speed ratio case ($U_\infty = 10.0\text{ m/s}$, $\lambda = 10.0$). The dashed lines indicate concentric circles of radius 1, 1.5 and 2 chord lengths about the local quarter chord of the DU91-W2-250 aerofoil section. The arbitrary mesh interface is located at $x/c = 2.68$.

drag polars for use in low order rotor models, the technique used should be as conceptually consistent as possible with the method used to obtain the angle of attack in the low order rotor model, when sampling the flow field.

In the MEXICO project several methods have been attempted to compute the angle of attack and relative velocity, including inverse free wake, direct wake reconstruction, inverse blade element momentum and azimuthal average induction factor methods [4]. Unfortunately, these methods did not show good agreement in the final MEXICO report and none of the methods were deemed to be universally superior [4]. Likewise, several methods have been proposed in the literature to extract 3D aerofoil characteristics from a rotating blade, such as those of Bak et al. [20] and Shen et al. [21]. In this study, the azimuthal average induction factor method of Johansen and Sørensen [22] was found to be the most reliable method and was adopted to derive the lift and drag polars. This method computes the angle of attack and relative velocity based on the integrated axial and swirl velocities through a separate annulus containing each spanwise section of the blade. Other methods based on sampling the local flow field were found to be less reliable because, particularly near the blade root and at high tip speed ratios, the wake of the upstream blade was found to pass in close proximity with the downstream blade. Fig. 10 shows contours of the lateral velocity U_y (relative to the blade) on a horizontal slice through the blade at a spanwise distance of $r/R = 0.25$, for the design tip speed ratio ($U_\infty = 15.0\text{ m/s}$, $\lambda = 6.67$) and high tip speed ratio cases ($U_\infty = 10.0\text{ m/s}$, $\lambda = 10.0$). For the design tip speed ratio, the wake of the upstream blade caused a visible distortion to the local flow field around the aerofoil section, even for distances as close as 1.5 chord lengths away. For the high tip speed ratio case, the wake from the upstream blade passed even closer to the aerofoil, with visible distortions up to 1 chord length away. Hence methods based on sampling the local flow field were found to be sensitive to the exact location of the sample point and were therefore deemed to be too unreliable. Whilst still sub-optimal, the azimuthal average induction factor method did not suffer from this drawback.

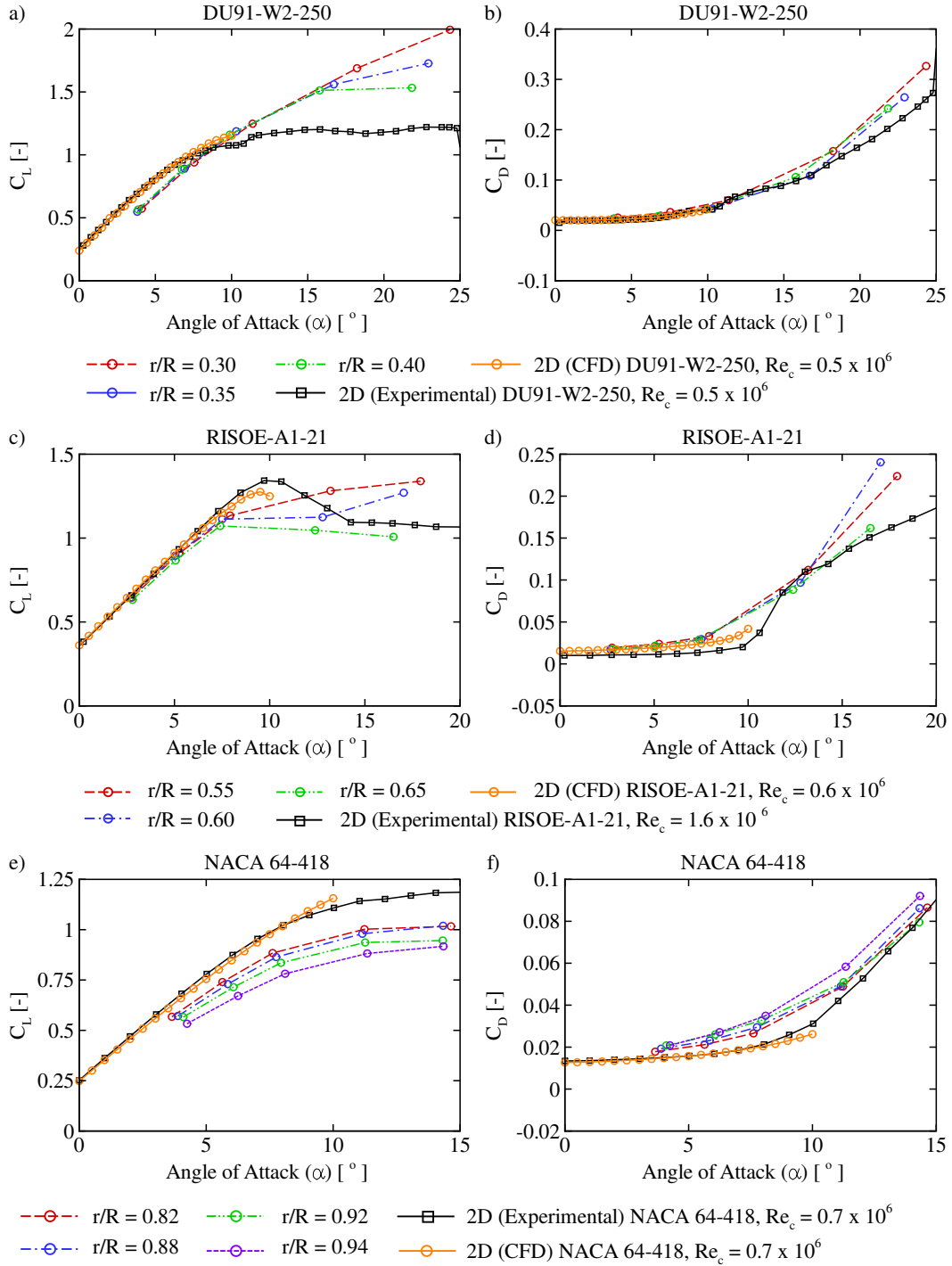


Figure 11. Lift and drag coefficients extracted from the blade resolved computations for several spanwise sections of the MEXICO rotor. The chord based Reynolds number is between 4.4×10^5 and 5.7×10^5 for the DU91-W2-250 sections ($r/R = 0.3, 0.35, 0.4$), between 5.7×10^5 and 6.4×10^5 for the RISØ-A1-21 sections ($r/R = 0.55, 0.6, 0.65$) and between 6.1×10^5 and 6.6×10^5 for the NACA64-418 sections ($r/R = 0.82, 0.88, 0.92, 0.94$).

Fig. 11 shows the lift and drag polars extracted from the blade resolved computations for the medium mesh. Also shown for comparison are the 2D experimental lift and drag polars for the DU91-W2-250 at a chord based Reynolds number

$Re_c = 0.5 \times 10^6$, the RISØ-A1-21 at $Re_c = 1.6 \times 10^6$ and the NACA 64-418 at $Re_c = 0.7 \times 10^6$ [4]. However, the chord based Reynolds number for the RISØ-A1-21 blade sections on the MEXICO rotor was found to be much lower than the chord based Reynolds number adopted for the 2D aerofoil section experiments. Therefore, additional 2D CFD computations were performed for the aerofoil sections at more appropriate Reynolds numbers of $Re_c = 0.5 \times 10^6$ for the DU91-W2-250, $Re_c = 0.6 \times 10^6$ for the RISØ-A1-21 and $Re_c = 0.7 \times 10^6$ for the NACA 64-418. The results of these computations are also shown in Fig. 11.

Comparing the 3D polars extracted from the blade resolved computations and the 2D polars calculated both computationally and experimentally, allowed the 3D effects associated with the rotating blade to be identified. For the inboard DU91-W2-250 sections (from $r/R = 0.20$ to $r/R = 0.46$), the maximum lift coefficient was found to increase far above that predicted by the 2D computations. On the other hand, the drag coefficient was found to be almost the same as the 2D computations and experimental values. The phenomena of increasing maximum lift coefficient near the blade root has historically been attributed to the strong centrifugal and coriolis forces, resulting in stall delay [23]. For stall regulated rotors, stall delay is often accounted for empirically in BEM codes by a correction factor of the form given by Snel [23], Du and Selig [24] or Chaviaropolous and Hansen [25], which seek to reproduce the same qualitative behaviour shown here.

Along the blade mid-span, the RISØ-A1-21 sections (from $r/R = 0.54$ to $r/R = 0.66$) were sufficiently far from both the root and the tip for 3D effects to be less significant. As a result, both the lift and drag coefficients showed negligible change between the 3 considered spanwise stations ($r/R = 0.55, 0.60, 0.65$) and good agreement with the 2D computational values, before the onset of stall. Hence the spanwise flow component was deemed to have negligible effect on the performance of the blade mid-span. However, both the 3D extracted and 2D computational drag coefficients were found to be greater than the 2D experimental drag coefficients. A further set of 2D aerofoil computations confirmed this to be due to the higher Reynolds number of the experiments (1.6×10^6) than the 2D computations (0.6×10^6) and that experienced by the 3D blade sections (0.57×10^6 to 0.64×10^6). After the onset of stall, it should be emphasised that the steady MRF approach was not able to capture the unsteady separation process accurately, as shown previously in Fig. 5. The data points (and the line segments between them) for the RISØ-A1-21 sections at high angles of attack, are therefore only shown in Fig. 11 for completion and should not be interpreted in further detail.

As the actuator line computations were performed before the onset of stall, the lift and drag polars for the blade outboard sections were of paramount importance, as this region of the blade was the main contributor towards the rotor thrust and torque. With increasing spanwise distance along the blade outboard sections (from $r/R = 0.82$ to $r/R = 0.94$), the lift coefficients for the NACA 64-418 sections showed a clear decrease and the drag coefficient a small increase, when compared with the 2D computational and experimental values. This phenomena is currently attributed to the pressure equalisation that occurs between the pressure and suction surface at the blade tip and is commonly accounted for by a 'pressure equalisation' correction of the form given by Shen et al. [7]. For their correction factor, the axial and tangential forces per unit span were multiplied by a factor F_1 before computing the total force applied to the flow field.

$$F_1(r) = \frac{2}{\pi} \cos^{-1} \left[\exp \left(-g_1 \frac{N(R-r)}{2r \sin[\phi(r)]} \right) \right] \quad (6)$$

$$g_1 = \exp(-c_1(N\lambda - c_2)) + 0.1 \quad (7)$$

In equations 6 and 7, N represents the number of blades and $c_1 = 0.125$ and $c_2 = 21.0$ represent empirical constants that were originally determined by curve fitting to experimental data from the NREL Phase VI rotor at a low tip speed ratio ($\lambda = 3.79$) and the Swedish WG 500 rotor at a high tip speed ratio ($\lambda = 14.00$). As the constants were not originally calibrated for the MEXICO rotor, the performance of the correction factor is not expected to be as applicable here. Therefore, an additional attempt was made to calibrate the empirical coefficients (c_1 and c_2) to the MEXICO rotor. To compute the new empirical coefficients, the blade resolved forces per unit span (F_{ax}^{BR} and F_t^{BR}) were used to represent the forces per unit span acting on the blade with pressure equalisation effects included. Whereas the actuator line forces per unit span (F_{ax}^{AL} and F_t^{AL}), computed based on the 2D simulated lift and drag coefficients with no empirical correction factors, were used to represent the forces per unit span acting on the blade with no pressure equalisation effects included. Hence the ratio between the two sets of forces per unit span ($F_{1,ax}$ and $F_{1,t}$) represented the reduction in axial and tangential forces per unit span along the blade outboard sections, due to pressure equalisation at the blade tip.

$$F_{1,ax}(r) = \frac{F_{ax}^{BR}(r)}{F_{ax}^{AL}(r)} \quad (8)$$

$$F_{1,t}(r) = \frac{F_t^{BR}(r)}{F_t^{AL}(r)} \quad (9)$$

The coefficients c_1 and c_2 were then fitted (through residual minimisation) to map the Shen et al. empirical correction factor to each of the target ratios $F_{1,ax}$ (Equation 8) and $F_{1,t}$ (Equation 9) separately; see Fig. 12. During the mapping

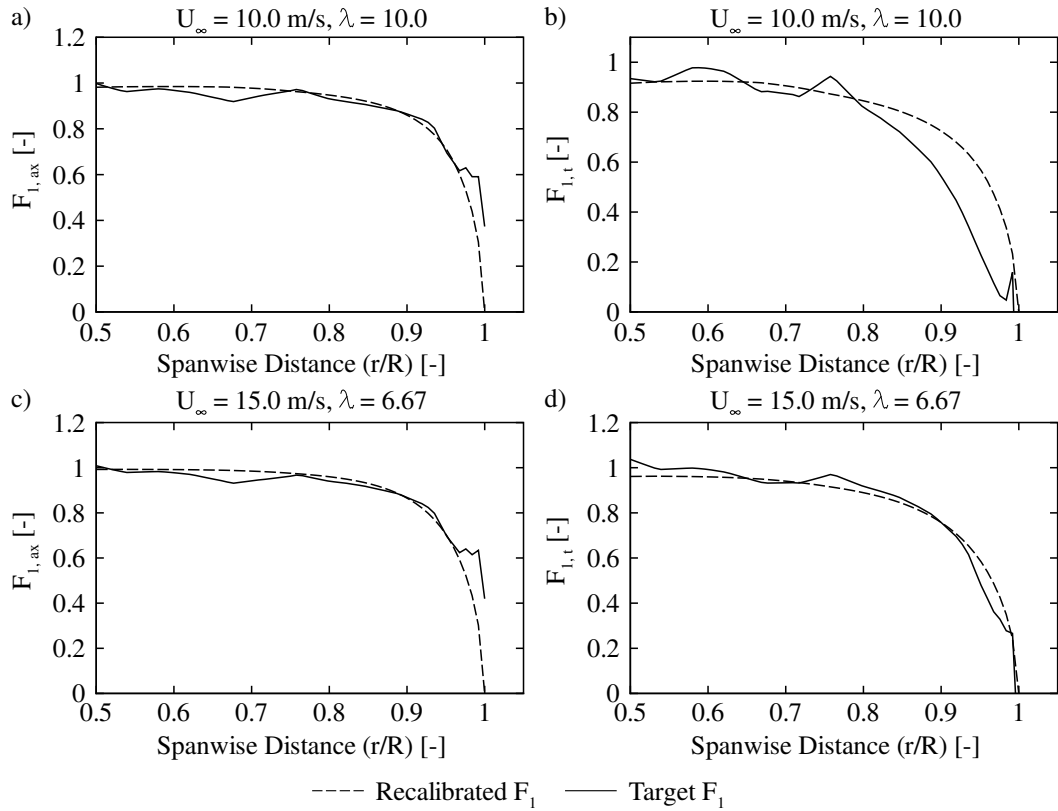


Figure 12. Mapping of recalibrated F_1 to target F_1 for the axial (a and c) and tangential (b and d) forces per unit span, for the high tip speed ratio case ($U_\infty = 10.0\text{ m/s}$, $\lambda = 10.0$) and the design tip speed ratio case ($U_\infty = 15.0\text{ m/s}$, $\lambda = 6.67$).

process, only the outboard sections of the blade (between $r/R = 0.80$ and 0.95) and the root and tip boundary conditions were used, as this correction factor was only intended to capture the effect of pressure equalisation on the blade outboard sections. The blade tip region ($r/R > 0.95$) showed inconsistent trends and was therefore excluded from the mapping.

Based on the curve fits computed at the design tip speed ratio ($U_\infty = 15.0\text{ m/s}$, $\lambda = 6.67$) and high tip speed ratio ($U_\infty = 10.0\text{ m/s}$, $\lambda = 10.0$) operating conditions, the empirical coefficients (c_1 and c_2) were determined to be 0.093 and 21.4 when based on the axial force per unit span ($F_{1,ax}$) and 0.123 and 19.2 when based on the tangential force per unit span ($F_{1,t}$). While both sets of coefficients were in the region of the original coefficients proposed by Shen et al. [1] (0.125 and 21.0), the coefficients required for the axial and tangential forces per unit span were found to be different. This is because (at least for the MEXICO rotor considered here) pressure equalisation was found to cause a greater reduction in tangential force per unit span than in axial force per unit span, as shown in Fig. 12. Conventional application of the tip correction factor of Shen et al. uses the same empirical coefficients in the axial and tangential directions. The observations presented here suggest that a different set of empirical coefficients may be required for the axial and tangential forces per unit span, depending on the rotor. However, further examination of the structure of the empirical correction factor was beyond the scope of this study and was therefore not carried out. Instead, the lift and drag polars extracted from the blade resolved computations (shown in Fig. 11) are input directly into an actuator line method, thus avoiding the need for any empirical correction factors. A comparison is then made with the experimental measurements and the original blade resolved computations from which they were derived.

7. ACTUATOR LINE COMPUTATIONS

The derived aerodynamic polars were used as inputs for actuator line computations of the MEXICO rotor, the code being implemented as an additional shared object library within OpenFOAM (version 2.3.1). The code adopts the potential flow equivalence method of Schluntz and Willden [26] for sampling the velocity field returned by the flow solver and the Gaussian smearing technique of Sørensen and Shen [27] to reapply the blade forces to the flow field. Further details of the

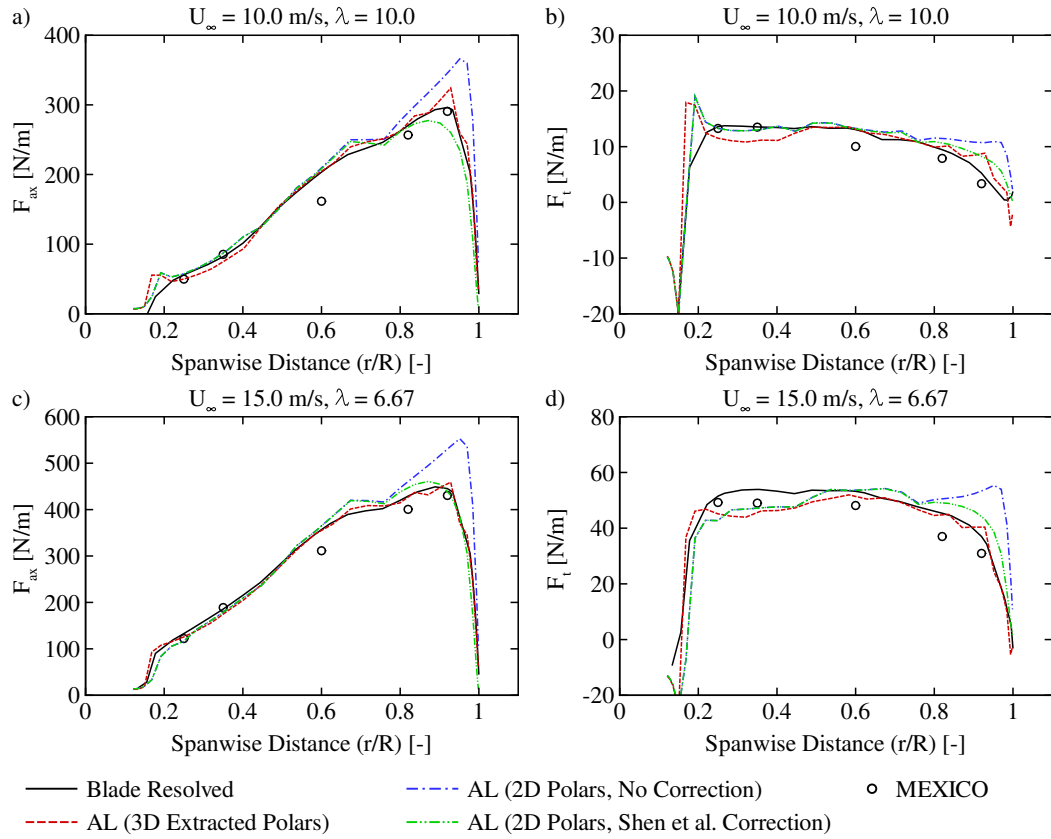


Figure 13. Axial and tangential blade forces computed using the actuator line (AL) method for freestream velocities of 10.0 m/s (a and b) and 15.0 m/s (c and d).

code implementation, validation and sensitivity to mesh refinement can be found in Wimshurst and Willden [19]. Smearing the blade force over multiple cells was necessary to avoid numerical instabilities associated with the application of high force densities to the flow field, that result in non-physical velocity gradients. However, Martínez-Tossas et al. [2] and Jha et al [3] (amongst others) have demonstrated that the accuracy of the computed blade loading can be strongly dependant on the smearing parameter ϵ , used to control the width of the Gaussian distribution and consequently the number of cells that the force is smeared over. In this study, a constant value of half the average chord ($0.5 \times 13.4\text{cm} = 6.7\text{cm}$) was adopted for the smearing parameter along the entire blade span. This follows a previous sensitivity study reported by Wimshurst and Willden [19], in which it was found that the solution was relatively insensitive for $\epsilon < c_{avg}$ (where c_{avg} is the average chord). It should be emphasised that both the smearing parameter and the aerodynamic polars can significantly affect the accuracy of the computed blade loads and both require careful consideration. However the focus of this investigation was the aerodynamic polars and hence the effect of the smearing distribution was not considered further.

Actuator line computations were carried out at the high tip speed ratio ($U_{\infty} = 10.0\text{m/s}$, $\lambda = 10.0$) and design ($U_{\infty} = 15.0\text{m/s}$, $\lambda = 6.67$) operating conditions, using three sets of aerodynamic polars. The first set of polars were extracted from the blade resolved computations in the previous section. The second set of polars were taken from the 2D CFD computations of the isolated non-rotating aerofoil sections without empirical corrections and the third set also adopted the 2D computational values but with the empirical ‘pressure equalisation’ correction factor of Shen et al. [7], with the original empirical constants ($c_1 = 0.125$, $c_2 = 21.0$).

Fig. 13 compares the results of all three sets of actuator line computations with the original experimental measurements and the blade resolved computations. When interpreting the results in Fig. 13, the blade resolved computations should be taken as the target values for the actuator line computations, rather than the experimental measurements. This is because the blade resolved computations were previously deemed to be more reliable, due to the uncertainties in the chordwise and spanwise integration of the experimental measurements, as a result of the sparsity of the pressure taps. The experimental values are therefore only shown in Fig. 13 for reference. Without any empirical correction factors, the actuator line computations with the 2D lift and drag polars significantly over-predicted both the axial and tangential forces for the

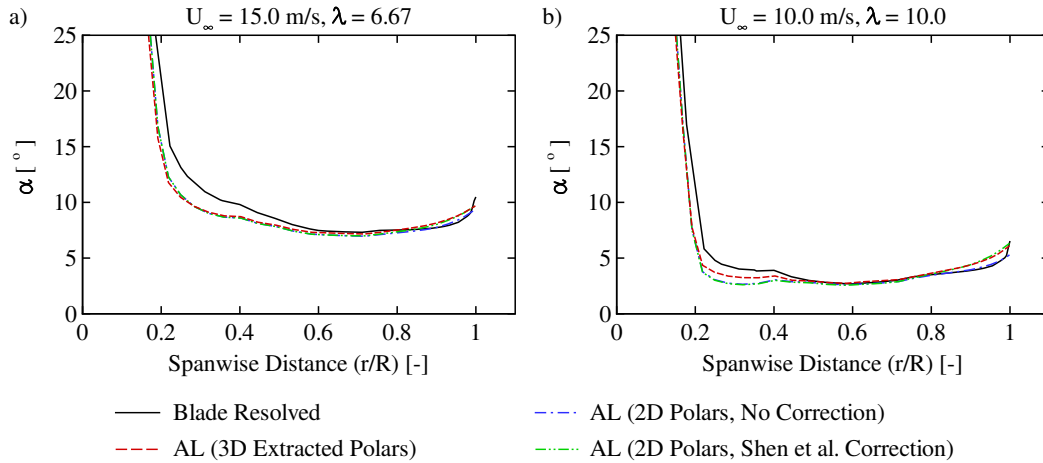


Figure 14. Angle of attack variation computed along the blade span for (a) the design tip speed ratio case ($U_{\infty} = 15.0 \text{ m/s}$, $\lambda = 6.67$) and (b) the high tip speed ratio case ($U_{\infty} = 10.0 \text{ m/s}$, $\lambda = 10.0$). Blade resolved data is from post computation analysis of the flow field, whilst actuator line data is computed from the blade element calculation during the computation.

outboard sections ($r/R > 0.8$). The inclusion of the Shen et al. [7] correction factor did lead to a definite improvement in both the axial and tangential forces for the outboard sections, however it was clear that this correction factor was still sub-optimal. As expected, the closest agreement with the blade resolved computations for the outboard sections was obtained with the actuator line method using the lift and drag polars derived from the blade resolved computations. This is because the change in lift and drag coefficients on the outboard sections due to pressure equalisation at the blade tip, was better represented by using the polars extracted directly from the blade resolved computations, rather than an inappropriately calibrated empirical correction factor.

However, further examination of the spanwise forces in Fig. 13 showed that the actuator line computations with the lift and drag polars derived from blade resolved CFD did not give universal agreement with the blade resolved computations. In particular, the axial and tangential forces for the blade inboard sections ($r/R < 0.45$) were both under-predicted using this method. To help identify the cause of this discrepancy, Fig. 14 shows the angle of attack computed along the blade span for the blade resolved and actuator line computations at the design tip speed ratio ($U_{\infty} = 15.0 \text{ m/s}$, $\lambda = 6.67$) and high tip speed ratio cases ($U_{\infty} = 10.0 \text{ m/s}$, $\lambda = 10.0$). As shown in Fig. 14, all of the actuator line computations under-predicted the angle of attack on the inboard sections, which ultimately resulted in the under-prediction of the axial and tangential forces shown in Fig. 13. This is because the actuator line method used the potential flow equivalence method of Schluntz and Willden [26] to sample the flow field and compute the angle of attack, whereas the blade resolved computations used the azimuthal average induction factor method of Johansen and Sørensen [22]. The potential flow equivalence method samples points in the plane of the aerofoil section at a distance of 1 chord length away from the quarter chord point, whereas the azimuthal average induction factor method uses a cylindrical annulus to determine the azimuthally averaged induction factor. As shown in Fig. 10, the wake of the upstream blade passed in close proximity to the downstream blade for the inboard sections, creating visible distortions to the local flow field. Hence, the assumption of a uniform free stream and a point vortex (used to sample the flow field in the potential flow equivalence method) is likely to lead to some errors in the angle of attack prediction. The actuator line and blade resolved computations showed good agreement for the outboard sections and increasingly weaker agreement for the inboard sections, with a difference of 2.7° at a spanwise distance of $r/R = 0.25$ from the rotor apex (corresponding to Fig. 10 (b)), for the high tip speed ratio case.

In future it may be possible to improve the method used to determine the angle of attack on the blade inboard sections and hence lead to better agreement between the actuator line and blade resolved computations. For example, this may involve reducing the sampling distance for the inboard sections in the actuator line method, in order to avoid interference from the wake of the upstream blade, particularly at high tip speed ratio. However both methods gave good agreement for the blade outboard sections, where the majority of the rotor thrust and torque was generated and was the region of primary focus for this investigation.

The effect of the spanwise distribution of axial and tangential forces per unit span on the integrated rotor thrust and torque can be seen in Table III and IV, where the blade resolved computations have been used to compute the percentage error for the actuator line computations. It should be emphasised that the spanwise variation of axial and tangential forces per unit span should always be used where possible to assess the accuracy of low order rotor models, rather than integrated thrust and torque. This is because an under-prediction of the axial or tangential forces per unit span in one area can be

Table III. Integrated rotor thrust and torque using the actuator line method for the high tip speed ratio case ($U_\infty = 10.0\text{m/s}$, $\lambda = 10.0$). Percentage errors are expressed relative to the blade resolved computations.

	Thrust [N]	Torque [Nm]	Thrust Error [%]	Torque Error [%]
Blade Resolved	978.5	70.7		
AL (3D Extracted Polars)	997.1	74.4	+1.87	+4.97
AL (2D Polars, Shen et al. Correction)	975.9	86.1	-0.27	+17.9
AL (2D Polars, No Correction)	1079.0	87.4	+10.3	+19.1

Table IV. Integrated rotor thrust and torque using the actuator line method at the design condition ($U_\infty = 15.0\text{m/s}$, $\lambda = 6.67$). Percentage errors are expressed relative to the blade resolved computations.

	Thrust [N]	Torque [Nm]	Thrust Error [%]	Torque Error [%]
Blade Resolved	1704.3	329.5		
AL (3D Extracted Polars)	1688.9	315.8	-0.90	-4.16
AL (2D Polars, Shen et al. Correction)	1696.8	346.3	-0.44	+5.00
AL (2D Polars, No Correction)	1814.0	366.6	+6.44	+11.3

offset by an over-prediction elsewhere, resulting in a deceptively small error in the integrated values and possibly leading to unjustified confidence in the computed results. Nevertheless, the integrated rotor thrust and torque are still useful to demonstrate the importance of the blade axial and tangential forces per unit span on the blade outboard sections, for determining the rotor performance.

Unsurprisingly the actuator line computations with the 2D lift and drag polars and no empirical correction gave the worst agreement with the blade resolved computations, with a maximum error of 10.3% in thrust and 19.1% in torque, for the high tip speed ratio case. This was primarily due to the significant over-prediction of the axial and tangential forces per unit span on the outboard sections, as the effect of pressure equalisation was not accounted for at all. The inclusion of the empirical correction factor of Shen et al. [1] with the original empirical coefficients ($c_1 = 0.125$ and $c_2 = 21.0$), did lead to a reduction in integrated thrust and torque error, due to a reduction in axial and tangential forces per unit span on the outboard sections. However, it was clear by comparing the spanwise force variation in Fig. 13 with the blade resolved computations, that this correction was still insufficient. In fact, the relatively small integrated thrust error (-0.27% at the high tip speed ratio and -0.44% at the design condition) was only coincidental, as the under-prediction of the axial force per unit span on the inboard sections happened to offset the over-prediction on the outboard sections.

The closest agreement with the blade resolved computations was obtained by the actuator line computations with the lift and drag polars extracted from the blade resolved computations, due to the improved prediction of the axial and tangential forces per unit span on the outboard sections. Furthermore the small under-prediction of the integrated rotor thrust (-0.90% at the design condition) and torque (-4.16% at the design condition) by the actuator line computations was mainly a result of the under-prediction of the axial and tangential forces per unit span on the blade inboard sections. This in turn was due to the angle of attack under-prediction shown in Fig. 14. Improvements to the procedure used to determine the angle of attack may help to address this in future computations and thus provide further improvement to the actuator line method for modelling the blade loading on real rotors.

8. CONCLUSIONS

The MRF approach has been successfully applied to compute high fidelity blade loading and near wake flow field data for a laboratory scale wind turbine rotor, demonstrating good agreement with the pressure coefficient and PIV data. Lift and drag polars were extracted from the computed data and subsequently used as inputs for actuator line computations of the same rotor. When compared to actuator line computations using 2D simulated aerodynamic data, the 3D extracted polar actuator line computations gave improved agreement with the blade resolved computations, particularly for the outboard sections. This is because the extracted lift and drag polars implicitly capture the effect of pressure equalisation at the blade tip by reducing the lift coefficient and increasing the drag coefficient on the outboard sections. Hence, the need to apply an empirical correction factor to the blade loading distribution is negated. The improved agreement on the blade outboard sections leads to a subsequent improvement in integrated rotor thrust and torque prediction.

The blade inboard sections were found to give weaker agreement between the actuator line and blade resolved computations. This was attributed to errors in the angle of attack prediction, caused by distortions to the local flow field

from the upstream blade wake. These errors may increase at high tip speed ratios and for high solidity rotors. It is suggested that locally reducing the sampling distance around the aerofoil section may be used to reduce this source of error.

As an alternative approach, the data from the blade resolved computations was also used to derive modified empirical coefficients for the spanwise loading correction factor of Shen et al. [1]. Although the computed coefficient values were in the region of the original coefficients, it was found that different coefficient values were required in the axial and tangential directions. These observations suggest that although different empirical coefficients may be required for different rotors, the original coefficients of Shen et al. may be a reasonable first approximation.

ACKNOWLEDGEMENT

The author would like to thank Uniper and EPSRC for funding the CASE-Studentship for this project and the Advanced Research Computing (ARC) facility at the University of Oxford where the computations were performed. The author would also like to thank the consortium which carried out the EU FP5 project MEXICO: 'Model Rotor Experiments in Controlled Conditions' to which 9 European partners contributed. They provided a computer aided design (CAD) file containing the geometry of the MEXICO blade that was used to generate the blade resolved mesh of the MEXICO rotor.

REFERENCES

1. Shen WZ, Mikkelsen R, Sørensen JN. Tip loss corrections for wind turbine computations. *Wind Energy* 2005; **8**:457–475.
2. Martínez-Tossas L, Churchfield M, Leonardi S. Large eddy simulations of the flow past wind turbines: actuator line and actuator disc modelling. *Wind Energy* 2015; **18**:1047–1060.
3. Jha P, Churchfield M, Moriarty P, Schmitz S. Accuracy of state-of-the-art actuator-line modeling for wind turbine wakes. *51st AIAA Aerospace Sciences Meeting including the New Horizons Forum and Aerospace Exposition*, AIAA: Grapevine (Dallas/Ft. Worth Region), Texas, 2013; AIAA 2013–0608.
4. Schepers JG, Boorsma K, Cho T, Gomez-Iradi S, Schaffarczyk P, Jeromin A, Shen WZ, Lutz T, Meister K, Stoevesandt B, *et al.*. Final report of IEA task 29, Mexnext (phase 1): Analysis of MEXICO wind tunnel measurements. *Technical Report ECN-E12-004*, Energy Research Centre of the Netherlands (ECN) February 2012.
5. Boorsma K, Schepers JG. New MEXICO experiment: Preliminary overview with initial validation. *Technical Report ECN-E-14-048*, Energy Research Centre of the Netherlands (ECN) September 2014.
6. Boorsma K, Schepers JG. Description of experimental setup, MEXICO measurements. *Technical Report ECN-X-09-0XX*, Energy Research Centre of the Netherlands (ECN) 2009.
7. Shen WZ, Zhu WJ, Sørensen JN. Actuator line/Navier-Stokes computations for the MEXICO rotor: comparison with detailed measurements. *Wind Energy* 2012; **15**:811–825.
8. Hand MM, Simms DA, Fingersh LJ, Jager DW, Cotrell JR, Schreck S, Larwood SM. Unsteady aerodynamic experiment phase VI: Wind tunnel test configurations and available data campaigns. *Technical Report NREL/TP-500-29955*, National Renewable Energy Laboratory (NREL) 2001.
9. Bechmann A, Sørensen N, Zahle F. CFD simulations of the MEXICO rotor. *Wind Energy* 2011; **14**:677–689.
10. Nishino T, Willden RHJ. Effects of 3-D channel blockage and turbulent wake mixing on the limit of power extraction by tidal turbines. *International Journal of Heat and Fluid Flow*. 2012; **37**:123–135.
11. Farrell PE, Maddison JR. Conservative interpolation between volume meshes by local galerkin projection. *Comput. Methods Appl. Mech. Engrg.* 2011; **200**:89–100.
12. Luo JY, Issa RI, Gosman AD. Prediction of impeller-induced flows in mixing vessels using multiple frames of reference. *ICHEME Symposium Series*, 136, 1994; 549–556.
13. Rhie CM, Chow WL. Numerical study of turbulent flow past an aerofoil with trailing edge separation. *AIAA journal* 1983; **21**:1525–1532.
14. Patankar SV. *Numerical Heat Transfer and Fluid Flow*. Hemisphere Publishing Corporation: Washington DC (USA), 1980.
15. Sweby PK. High resolution schemes using flux limiters for hyperbolic conservation laws. *SIAM Journal on Numerical Analysis* 1984; **21**:995–1011.
16. Menter FR. Two-equation eddy-viscosity turbulence models for engineering applications. *AIAA Journal* 1994; **32**(8):1598–1605.
17. Menter FR, Kuntz M, Langtry R. Ten years of industrial experience with the SST turbulence model. *Turbulence, Heat and Mass Transfer* 2003; **4**:625–632.
18. Jasak H. Error analysis and estimation for the finite volume method with applications to fluid flows. PhD Thesis, Imperial College London 1996.

19. Wimshurst A, Willden RHJ. Validation of an actuator line method for tidal turbine rotors. *The 26th International Ocean and Polar Engineering Conference*, ISOPE: Rhodes (Rodas), Greece, 2016; TPC-2016-0825.
20. Bak C, Johansen J, Andersen P. Three dimensional corrections of airfoil characteristics based on pressure distributions. *European Wind Energy Conference & Exhibition (EWEC)*, EWEA: Athens, Greece, 2006.
21. Shen W, Hansen M, Sørensen JN. Determination of the angle of attack on rotor blades. *Wind Energy* 2009; **12**:91–98.
22. Johansen J, Sørensen NN. Aerofoil characteristics from 3D CFD rotor computations. *Wind Energy* 2004; **7**:283–294.
23. Snel H, Van Holten T. Review of recent aerodynamic research on wind turbines with relevance to rotorcraft. *Aerodynamics and Aeroacoustics of Rotorcraft*, AGARD CP-552, Berlin, Germany, 1994; 139–149.
24. Du Z, Selig M. A 3-D stall-delay model for horizontal axis wind turbine performance prediction. *AIAA Paper* 1998; **21**:9–19.
25. Chaviaropoulos PK, Hansen MOL. Investigating three-dimensional and rotational effects on wind turbine blades by means of a quasi-3d navier-stokes solver. *Journal of Fluids Engineering* 2000; **122**:330–336.
26. Schluntz J, Willden R. An actuator line based method with novel blade flow field coupling based on potential flow equivalence. *Wind Energy* 2015; **18**(8):1469 – 1485.
27. Sørensen JN, Shen WZ. Numerical modelling of wind turbine wakes. *Journal of Fluids Engineering* 2002; **124**(2):393–399.